



First-Principles Investigation of the Early-Stage Precipitations in Mg-Sn and Mg-Zn Alloys

Du Cheng, Kang Wang, and Bi-Cheng Zhou

Abstract

Mg-Sn and Mg-Zn alloys exhibit a strong age-hardening effect and have become promising bases for high-strength and low-cost Mg alloys. However, the atomic structures and phase stabilities of various precipitates and inter-metallic compounds during the heat treatment in these systems remain unclear. Here we use a combined approach of first-principles calculations and cluster expansion (CE) to investigate the atomic structures and thermodynamic stabilities of the experimentally reported precipitates as well as orderings on the FCC and HCP lattices in Mg-Sn and Mg-Zn alloys. From the low energy structures searched by CE, potential Guinier–Preston (GP) zones are identified from preferred HCP orderings. The slow convergence for CE of HCP Mg-Zn, compared with that of Mg-Sn system, is attributed to the long-ranged interactions resulting from the larger lattice mismatch. This study could help design better age-hardened Mg alloys.

Keywords

Mg-Sn • Mg-Zn • Precipitation • First-principles • Cluster expansion

Introduction

Magnesium (Mg) is the lightest engineering metal with a density of $\sim 1.7 \text{ g/cm}^3$, which is significantly lower than aluminum (Al, 2.7 g/cm^3), titanium (Ti, 4.5 g/cm^3), and iron

(Fe, 7.9 g/cm^3), thus becomes a promising candidate for weight reduction materials in vehicles. Comprising 2.7% of the earth's crust, Mg is the most abundant metallic element and can be readily commercially produced from seawater and ores with a purity that can exceed 99.8% [1], thus providing ample resources to cover the use of its alloys in various engineering sectors. Apart from lightness and abundance, Mg alloys have shown a high strength-to-weight ratio among structural alloys, excellent castability, recyclability, versatility in processing (e.g., rolling, extrusion and machining), exceptional dampening capacity, non-toxicity towards the environment and the human body, etc. [1]. Because of such attractive features, Mg alloys have received considerable research over the last decade for potentially wider and larger applications in the automotive, aircraft, aerospace, and 3C (computer, communication, and consumer electronic product) industries [2]. Despite the considerable efforts made thus far, the adoption of Mg alloys in engineering applications remains limited compared with that achieved for Al alloys, mainly due to the inadequacies in yield strength, creep-resistance, formability, and corrosion resistance [2].

Among various methods to improve mechanical properties of Mg alloys, additions of rare-earth (RE) elements are particularly attractive due to its significant effect on various mechanisms, including solid solution strengthening [3], enhanced pyramidal slip of $\langle c + a \rangle$ dislocations [4–6], formation of long-period stacking ordered strengthening phases [7, 8], weakening of the textures and improving formability [9–14]. However, disadvantages of the Mg-RE-based alloys are also apparent. The scarcity of RE elements significantly raises the cost, making large-quantity usage (usually $\sim 10 \text{ wt.}\%$) of Mg-RE alloys impractical in industry applications. The major advantage of Mg alloys, i.e., low weight, gradually loses due to the increased density of the Mg-RE alloys [15]. Therefore, to further expand the industrial application of Mg alloys, development of

D. Cheng · K. Wang (✉) · B.-C. Zhou (✉)
Department of Materials Science and Engineering, University of Virginia, Charlottesville, VA 22904, US
e-mail: kw7rr@virginia.edu

B.-C. Zhou
e-mail: bicheng.zhou@virginia.edu

low-cost, RE-free Mg alloys with high strength is strongly desired.

Among the RE-free Mg alloys, the Mg-Sn and Mg-Zn alloys are attractive due to their precipitation hardenability and biocompatibility [1, 2, 16, 17]. The Mg-Sn-based alloys are promising for structural applications due to high solubility of Sn in Mg (i.e., 14.5 wt.% at 561 °C) [18], precipitate hardenability by β Mg₂Sn phase [2], and good castability resulting from the eutectic reaction at 561 °C [18]. Despite its merits, the strengthening Mg₂Sn phase usually has a coarse distribution and lies on the basal plane of Mg matrix [19] or at the grain boundaries of as-cast Mg-Sn alloys [20]. Due to its equilibrium nature, it takes a long time (e.g., weeks) to reach peak hardness [21, 22]. A detailed study of the microstructures of cast and solutionized Mg-9.8Sn (wt.%) alloy showed the presence of Guinier–Preston (G.P.) zones and coherent precipitates with L1₂ structure [23, 24]. The D0₁₉ Mg₃Sn phase is observed in as-solidified microstructures of Mg-1.5Sn (at.%) and Mg-9.76Sn (wt.%) alloys [25, 26]. However, the detailed structures and stability of these metastable phases (i.e., various G.P. zones, L1₂ and D0₁₉ Mg₃Sn) and their relations during the precipitation process remain unclear.

In Mg-Zn system, the maximum solubility of Zn in Mg matrix is 2.4 at.% at 613 K (340 °C) [2, 27], which decreases rapidly with lowering temperature and leads to supersaturated solid solution. Aging treatment leads to the formation of various precipitates that impede the movement of dislocations and improves the strength of the alloy. Mg and Zn species can be absorbed by the human body, and bivalent ions of Mg and Zn are essential for human metabolism [16, 28]. If the absorption rate is properly tuned, Mg-Zn alloys could become a promising candidate for various implants (e.g., bone screws, cardiovascular stent) [28]. Over the years, numerous efforts have been made to understand and tune the microstructures of Mg-Zn alloys since the discovery of its aging hardening effect [2]. Currently, the structures and stabilities of the phases in Mg-Zn system are not well understood, especially the exact stoichiometry and details of the atomic structure during the early stages of aging treatment [2].

In the current work, the phase structures and stabilities in the precipitation process of Mg-Sn and Mg-Zn alloys are investigated: a combined first-principles approach, i.e., cluster expansion (CE) [29, 30] and Monte Carlo (MC) [31] parameterized by energies from first-principles calculations based on density functional theory (DFT) [32, 33]. The computational methodology and parameters are detailed in Sect. “[Computational Methods](#)”. The results and analysis for Mg-Sn and Mg-Zn systems are shown in Sects. “[Precipitation in Mg-Sn Alloys](#) and [Precipitation in Mg-Zn Alloys](#)”. The role of lattice mismatch on phase stability is discussed in Sect. “[Discussions](#)”. The conclusions are summarized in Sect. “[Conclusions](#)”.

Computational Methods

The current work focuses on atomic-scale ordering/clustering phenomena, and their effect on the early-stage precipitates. CE with total energy input from DFT is adopted to parameterize the configuration-dependent energy of the lattice model. The obtained CE formula is used to exhaustively search the low energy atomic configurations up to a certain size of structures, which can reveal the atomic structures and energies of potential coherent precipitates. The molecular dynamics is not chosen due to its innate limitations of time scale [34] and the unavailability of accurate interatomic potentials for Mg-Sn and Mg-Zn alloys.

First-principles calculations based on DFT were employed to calculate the ground-state structures and energies of ordering phases on HCP and FCC lattice of Mg-Sn and Mg-Zn alloys. The ion–electron interaction was described by the projector augmented plane-wave method [35] and the exchange–correlation functional was described by an improved general gradient approximation of Perdew–Burke–Ernzerhof [36], as implemented in the Vienna Ab-initio Simulation Package (VASP, version 5.4) [37, 38]. The energy cut-off of 400 eV or larger was adopted for the plane-wave expansion of the electronic wave functions. The Methfessel–Paxton technique was adopted with smearing parameter of 0.2 eV for integration over k points [39]. The Brillouin zone was sampled by Gamma-centered grids with the k points per reciprocal atom over 8,000. For all the configurations under consideration, all degrees of freedom for the cell (e.g., volume, shape, and atomic positions) are allowed to relax for structural optimization. To improve the accuracy of energy calculations, static calculations with the tetrahedron method incorporating Blöchl correction [40] were adopted after structural relaxations.

To analyze the effects of lattice mismatch on the coherent phase stability, the epitaxial deformation energies of HCP Mg on basal and $\{10\bar{1}0\}$ prismatic planes were calculated as a function of lattice parameters on epitaxial planes. Under epitaxial deformation, the lattice parameters on the epitaxial plane are fixed to maintain coherency while the lattice parameter perpendicular to the epitaxial plane is free to relax [41]. For the basal plane of HCP lattice, there is only one independent lattice parameter on the epitaxial plane. For other crystallographic planes, there are two independent lattice parameters [42]. To simplify the calculations, the c/a on epitaxial plane is fixed at the equilibrium value of HCP Mg when calculating the epitaxial deformation energies for $\{10\bar{1}0\}$ prismatic plane. To examine the extent of anharmonic lattice distortion, the energy data within 0.95–1.05 vicinity of the equilibrium lattice parameters were taken for the harmonic fitting and compared with DFT, assuming the

elastic response within 0.95–1.05 vicinity of equilibrium lattice parameter is harmonic [43].

The CE method is widely used to construct the Hamiltonian of different atomic configurations. In the current work, the MAPS code in Alloy Theoretic Automated Toolkit (ATAT) [44, 45] is adopted to generate various atomic configurations on lattice and perform the CE calculations for HCP and FCC Mg-Sn and Mg-Zn alloys throughout the whole concentration range. In Mg-Sn alloys, G.P. zones and $D0_{19}$ ordering on the basal plane of HCP lattice, and $L1_2$ ordering on FCC lattice were observed experimentally [23, 24, 26]. In Mg-Zn alloys, G.P. zones were observed on basal and prismatic planes of HCP lattice [46], and cubic $C15$ $MgZn_2$ that resembles FCC lattice was also reported [47]. Additionally, precipitate with high solute concentration will be formed if the precipitate is energetically favored and solute is enriched in local regions in the Mg matrix. Therefore, CEs on HCP and FCC lattices of both alloys are performed in the whole concentration range. In CE, the pair, triplet, and quadruplet clusters, in addition to empty and point clusters, are adopted up to a chosen cut-off distance and the corresponding effective cluster interactions (ECIs) are used to fit the energy from DFT calculations. All structures with up to 14 and 12 atoms are searched, respectively, to yield converged CE results for HCP and FCC. The CE results are then adopted to search for relatively stable orderings with energy less than 5 meV above the convex hull with solute concentration up to 25 at.% Sn in Mg-Sn system and 50 at.% Zn in Mg-Zn system. The criterion of 5 meV is chosen since it is approximately the error bar for the energies predicted by CE. The choice of clusters in CE is optimized to minimize the cross-validation, which is the averaged prediction error of the CE formula. Eventually, there are 228 and 317 coherent structures included in the training of ECIs for HCP and FCC lattices in Mg-Sn alloys. And the numbers of pair, triplet, and quadruplet clusters adopted in CEs of HCP and FCC Mg-Sn lattices are 11, 15, 0 and 23, 12, 16, respectively. The leave-one-out cross-validation (LOOCV) score are 0.0035 and 0.0031 eV/atom, respectively, for CE of HCP and FCC lattices in Mg-Sn alloys. For Mg-Zn alloys, there are 385 and 248 structures included in the training for CE of HCP and FCC lattices, and the LOOCV are 0.0040 and 0.0042 eV/atom, respectively. The numbers of pair, triplet, and quadruplet clusters adopted in CEs of HCP and FCC Mg-Zn lattices are 21, 10, 15 and 17, 12, 16, respectively. To improve the convergence, the extent of structural relaxation away from the ideal lattice were characterized using the distortion of lattice vectors, the structures with distortion parameter larger than 0.1 were excluded from cluster expansion [48]. The details of the CE for Mg-Sn and Mg-Zn alloys are reported in Refs. [40, 50]

Precipitation in Mg-Sn Alloys

In the CE calculations, the relaxed structures from DFT calculations are examined via the lattice distortion to determine whether the structures should be included in the fitting of ECIs [48]. In Fig. 1, the lattice distortions as a function of x_{Sn} and their distributions are shown for relaxation of HCP and FCC orderings. The lattice distortion becomes larger as x_{Sn} increases from zero, and then decreases as x_{Sn} approaches unit. At the middle region, the lattice distortions are significantly larger because the alloy prefers to stay in the lattice of the stable intermetallic compound Mg_2Sn , thus deviating from ideal HCP or FCC lattices. In comparison, the lattice distortion of HCP is generally larger than that of FCC, since the c/a ratio of HCP Mg and Sn are different and while FCC Mg and Sn, by definition, are cubic and free of distortion. For both HCP and FCC, the lattice distortion drops around 0.1. For consistency, this lattice distortion criterion is chosen to select relaxed structures for the training of ECIs, and those with distortion larger than 0.1 are excluded, which is recommended in ATAT [48].

The ECI energies for clusters and CE results for HCP and FCC are shown in Fig. 2, respectively, where the energies from DFT, the corresponding energies from CE prediction, the metastable and global convex hulls of formation energy are plotted, with the energies of HCP Mg and BCT Sn as references. The pair and triplet clusters are enough to depict the energies of orderings on the HCP lattice, while quadruplet clusters also contribute to the energies of the FCC lattice; see Fig. 2a, b. The size (or diameter) of the cluster is defined as the largest two-site distance of the clusters. In both cases, the magnitude of the ECI energy decreases with the increasing size of clusters. The cut-off distance for pair and triplet interactions for CE of HCP lattice are 7.82 and 5.54 Å, respectively, while that for the pair, triplet, and quadruplet interactions for FCC lattice are 13.92, 6.39, and 5.53 Å, respectively. As shown in the convex hulls of formation energies (Fig. 2c), $D0_{19}$ Mg_3Sn and B19 $MgSn$ are predicted to be on the HCP convex hull while $L1_2$ Mg_3Sn and $L1_0$ $MgSn$ are on the FCC convex hull. The $D0_{19}$ and $L1_2$ Mg_3Sn phases are identified on the metastable convex hull with energies 32 and 7 meV/atom above the global convex hull, respectively, which indicates that $L1_2$ is more stable than $D0_{19}$ Mg_3Sn .

The potential G.P. zones are searched by examining the coherent ordering phases on or slightly above (within 5 meV) the HCP and FCC metastable convex hull; see Fig. 3a–c. The primitive cells of the structures are indicated by the dashed red lines and the solute-rich G.P. zones are indicated using green rectangles. Since $D0_{19}$ ordering is on the HCP convex hull, many orderings resembling $D0_{19}$ with

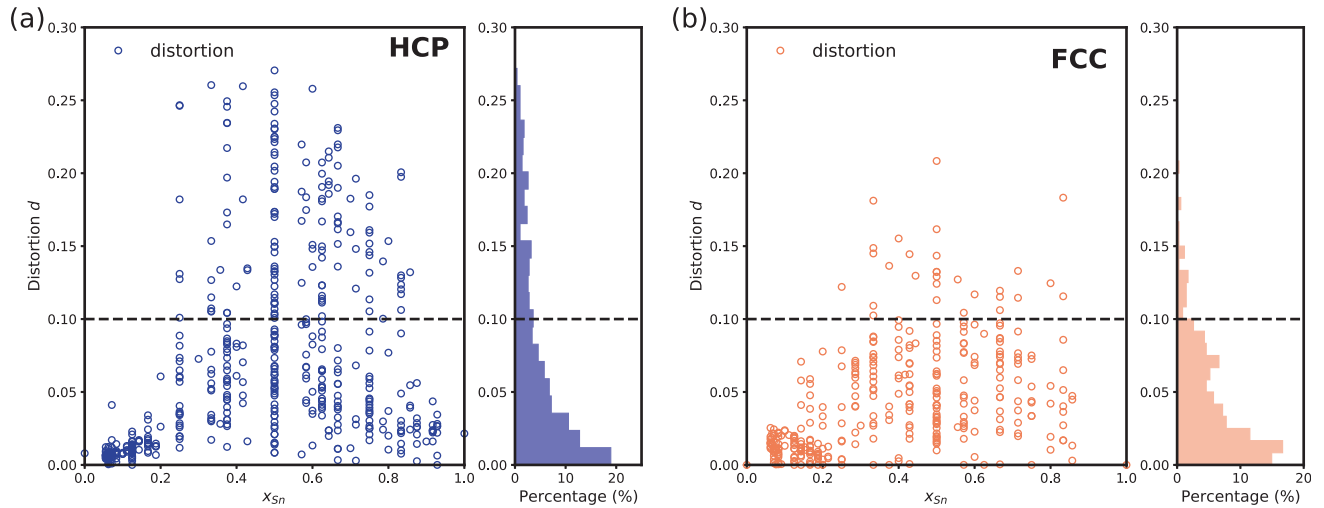


Fig. 1 Distortions of coherent orderings on HCP (a) and FCC (b) lattices of Mg-Sn alloys as a function of the molar fraction of Sn (left) and its histogram (right)

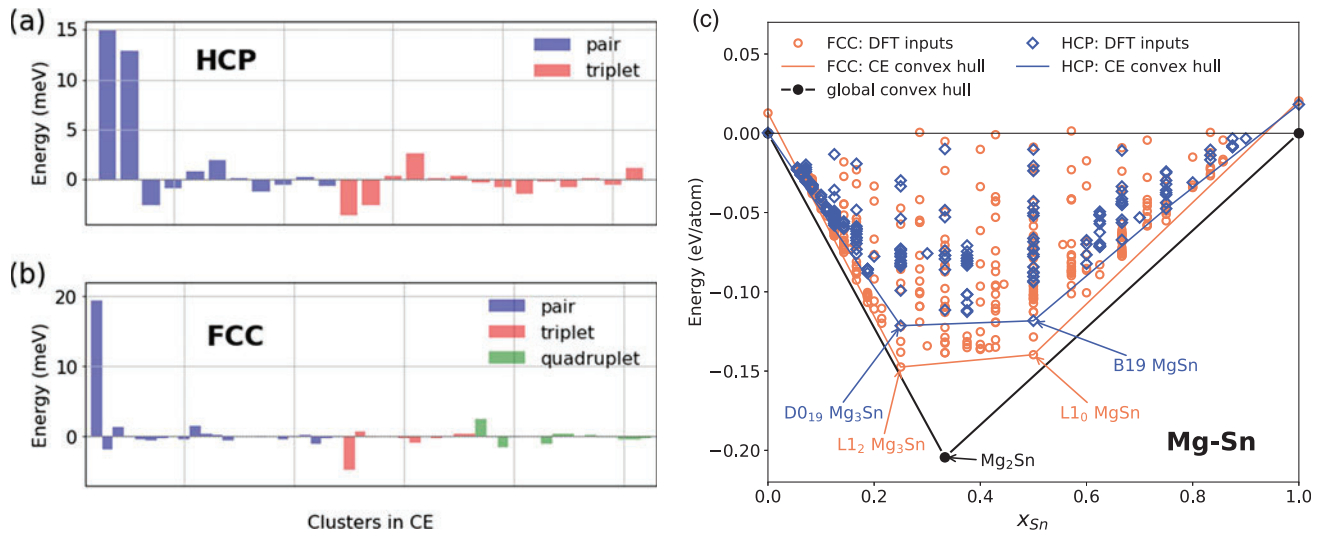


Fig. 2 Effective cluster interaction energies of the clusters in CE for HCP (a) and FCC lattices (b) of Mg-Sn alloys and the clusters are ordered with increasing size (largest two-site distance) within the

cluster. Formation energies of orderings (c) on the HCP and FCC lattices of Mg-Sn alloys from DFT calculations and the ground state convex hull

$x_{\text{Sn}} < 25$ at.% are also found. A potential G.P. zone on HCP lattice viewed along $[0001]$ and $[2\bar{1}\bar{1}0]$ are shown in Fig. 3a and b. Note that these zigzagged arrangements of Sn rods are the basic building blocks of the $D0_{19}$ phase, where such arrangements are stacked compactly with pure Mg. The popularity of such building block is reasonable from a thermodynamic perspective, considering that it is the basic unit of $D0_{19}$ on the HCP convex hull, and several layers of pure Mg are present between the basic units to maintain the overall concentration. Previous studies also revealed such zigzagged patterns of solute rods in Mg-based rare earth alloys, such as Mg-Nd [51] and Mg-Sc systems [52], where, similar to the current results, $D0_{19}$ structure with 25 at.%

solute is on the HCP convex hull of formation energies.

On FCC lattices of Mg-Sn alloys, many ordering phases with $x_{\text{Sn}} < 25$ at.% and slightly above (within 5 meV) the FCC metastable convex hull are identified in addition to $L1_2$ and $L1_0$. In Fig. 3c, a plate-like ordering on FCC lattice that resembles $L1_2$ ordering is shown along the $[001]$ direction. This type of atomic arrangement is common in the ordering phases with $x_{\text{Sn}} < 25$ at.% on FCC lattice. Similar to the orderings on HCP lattices, the coherent phases with $x_{\text{Sn}} < 25$ at.% on FCC lattice can be viewed as the mixture of Mg and $L1_2$ $Mg_3\text{Sn}$ on FCC lattice. Thus, local $L1_2$ $Mg_3\text{Sn}$ can be viewed as the building block of the coherent orderings on

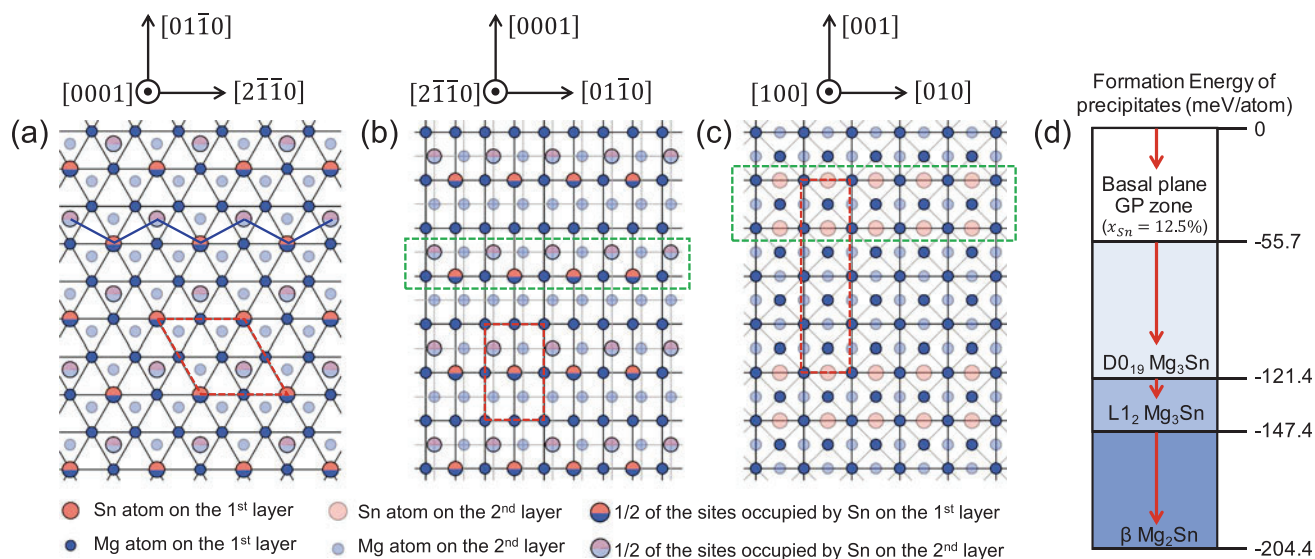


Fig. 3 Potential G.P. zones on HCP and FCC lattices of Mg-Sn alloys and the precipitation sequence. Potential G.P. zone on HCP lattice that resembles $D0_{19}$ viewed along $[0001]$ (a) and $[2\bar{1}\bar{1}0]$ (b) directions. Potential G.P. zone on FCC lattice that resembles $L1_2$ viewed along

$[100]$ direction. (d) The precipitation sequence in Mg-Sn alloys and the corresponding formation energies. The blue and red circles represent Mg and Sn atoms. The blue lines and green dashed rectangles indicate the Sn-rich region of the G.P. zone. The red dashed lines indicate the primitive cells (Color figure online)

FCC lattices. The plate-like $L1_2$ ordering is also observed experimentally [23].

With the identified potential G.P. zones on the basal plane with 12.5 at.% Sn and the energetics of $L1_2$ and $D0_{19}$ phases, the precipitation sequence can be described as supersaturated solid solution \rightarrow basal plane G.P. zones $\rightarrow D0_{19} Mg_3Sn \rightarrow L1_2 Mg_3Sn \rightarrow \beta Mg_2Sn$. The transition from $D0_{19}$ to $L1_2 Mg_3Sn$ can be facilitated by the appearance of stacking fault in HCP matrix. The evolution of the energetics of these phases is shown in Fig. 3d, which shows a decrease of the formation energies. From Fig. 2c, such an evolution of energetics agrees with the precipitation criterion by the monotonic decrease of the formation energies per solute atom [53].

Precipitation in Mg-Zn Alloys

The coherent structures on HCP and FCC lattices of Mg-Zn alloys were relaxed using DFT and the extent of lattice distortions are shown in Fig. 4. Similar to the case of Mg-Sn alloys, the lattice distortion increases with the solute concentration first, then decreases as x_{Zn} approaches 1. This is due to the fact that the stable phases (i.e., $C14 MgZn_2$, Mg_4Zn_7 , and $Mg_{21}Zn_{25}$) and the corresponding favored bonding are incoherent with the HCP and FCC lattices of Mg-Zn alloys. Compared with the Mg-Sn alloys, deviations of the orderings from FCC lattices are much more severe in Mg-Zn alloys, since a larger portion of the FCC orderings shows larger lattice distortion than 0.1. Note that there is an

experimentally observed FCC ordering (i.e., $L1_2$) in Mg-Sn system [23, 24], while none is found in Mg-Zn system. Hence the FCC orderings in Mg-Sn are more stable than those in Mg-Zn alloys, compared with the corresponding equilibrium phases. As for orderings on HCP lattices, the overly relaxed structures in Mg-Zn alloys include those related to $C14$ and $C15 MgZn_2$, which are observed experimentally [47]. Meanwhile, the HCP orderings excluded in the CE training for Mg-Sn alloys do not show clear connections to the experimentally observed phases.

The ECIs from CEs for HCP and FCC lattices are shown in Fig. 5a, b. Generally, the magnitude of ECI decreases with the increase in diameter of the cluster, which agrees with physical intuition that smaller clusters have larger energetic contributions. The cut-off distances for pair, triplet, and quadruplet clusters for CE of HCP lattice are 10.09, 5.52, and 5.52 Å, while for CE of FCC lattice are 12.78, 6.39, and 5.53 Å. Notice that a larger cut-off distance is required for the CE of HCP lattice for Mg-Zn alloys, compared with that of Mg-Sn alloys. Even with larger cut-off distances and more training structures, CE for HCP Mg-Zn alloys has larger LOOCV than that for Mg-Sn alloys. The slowed convergence could be due to the long-ranged interactions, which are not included in the CE due to the required cut-off distance.

The stabilities of the coherent orderings on HCP and FCC lattices, as well as the incoherent phases, are shown in Fig. 5c. On HCP lattice, the stable orderings include $B19 MgZn$ and $D0_{19} Mg_3Zn_3$, although $D0_{19} Mg_3Zn_3$ is only slightly above the HCP convex hull (2.7 meV/atom). The

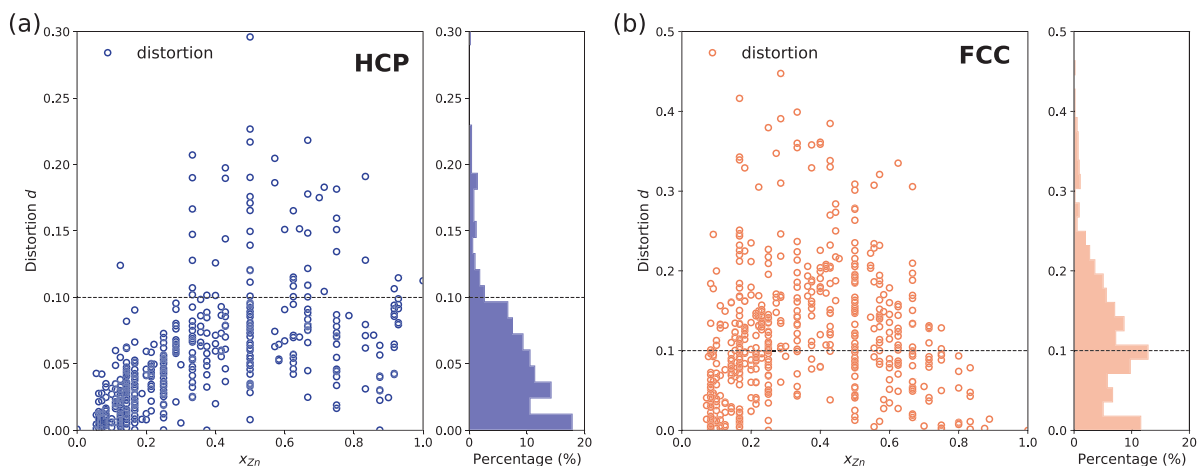


Fig. 4 Distortions of coherent orderings on HCP (a) and FCC (b) lattices of Mg-Zn alloys as a function of the molar fraction of Zn (left) and its histogram (right)

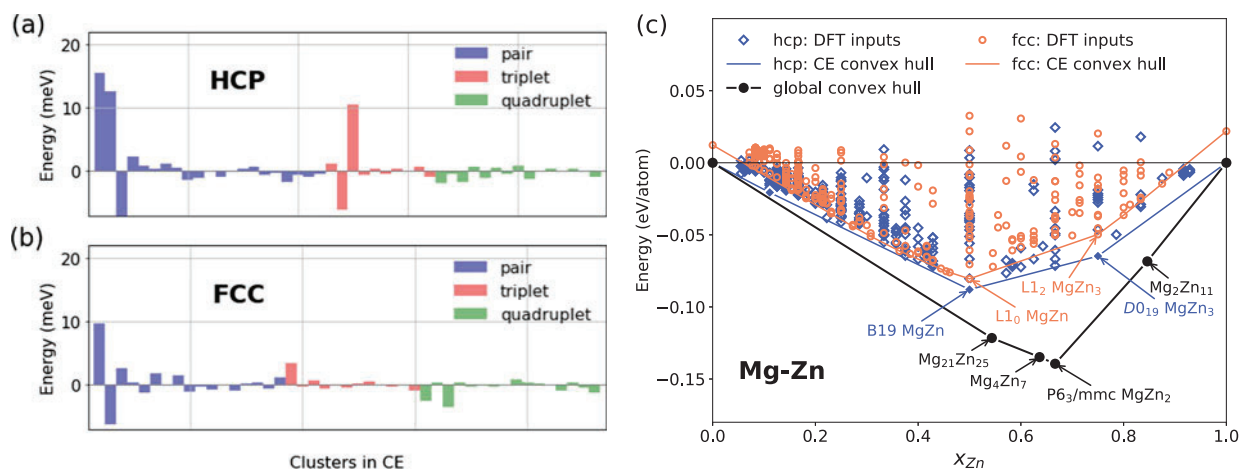


Fig. 5 Effective cluster interaction energies of the clusters in CE for HCP (a) and FCC lattices (b) of Mg-Zn alloys and the clusters are ordered with increasing size (largest two-site distance) of the cluster.

predicted stable phases include $\text{Mg}_{21}\text{Zn}_{25}$, Mg_4Zn_7 , C14 MgZn_2 , and $\text{Mg}_2\text{Zn}_{11}$, which agrees with the phase diagrams evaluated experimentally [54]. According to the criterion by Wang et al. [53], the precipitation sequence is related to the formation energy per solute atom, which can be visualized as the slope of the line connecting pure Mg and the corresponding phase. In the current calculations, the slopes for C14 MgZn_2 , Mg_4Zn_7 , and $\text{Mg}_{21}\text{Zn}_{25}$ are determined as -0.2091 , -0.2118 , and -0.2237 (eV/atom), thus leading to the stability sequence of C14 $\text{MgZn}_2 \rightarrow \text{Mg}_4\text{Zn}_7 \rightarrow \text{Mg}_{21}\text{Zn}_{25}$.

In Mg-Zn alloys, G.P. zones have been reported [46], although the experimental evidence is questioned and further examination with modern microscopy is needed [2]. From the CE for HCP lattice of Mg-Zn alloys, the coherent orderings close to HCP convex hull are searched to find

Formation energies of orderings (c) on the HCP and FCC lattices of Mg-Zn alloys from DFT calculations and the ground state convex hull

potential G.P. zones. In Fig. 6, the potential G.P. zones on basal, $\{01\bar{1}0\}$, and $\{2\bar{1}10\}$ planes are shown. The pink dashed lines indicate the primitive cell of the structures, and the blue rectangles indicate the solute-rich G.P. zones. The potential G.P. zone on basal plane has three atomic layers. The potential G.P. zone on $\{01\bar{1}0\}$ plane shows a similar structure to the B19 MgZn phase, which resides on the HCP convex hull. Notice that concentration of Zn is 100% in the Zn-rich layer of the identified G.P. zones on $\{01\bar{1}0\}$ plane. This could cause strong local lattice distortion and the local Zn layers may evolve to other incoherent and more stable phases. The lattice distortion is not incorporated in the CE approach. In contrast to the G.P. zone in Fig. 7b, the Zn concentrations in the Zn-rich layers of G.P. zones in Fig. 7a, c is only 50%, which are more likely to stay coherent with the HCP Mg matrix.

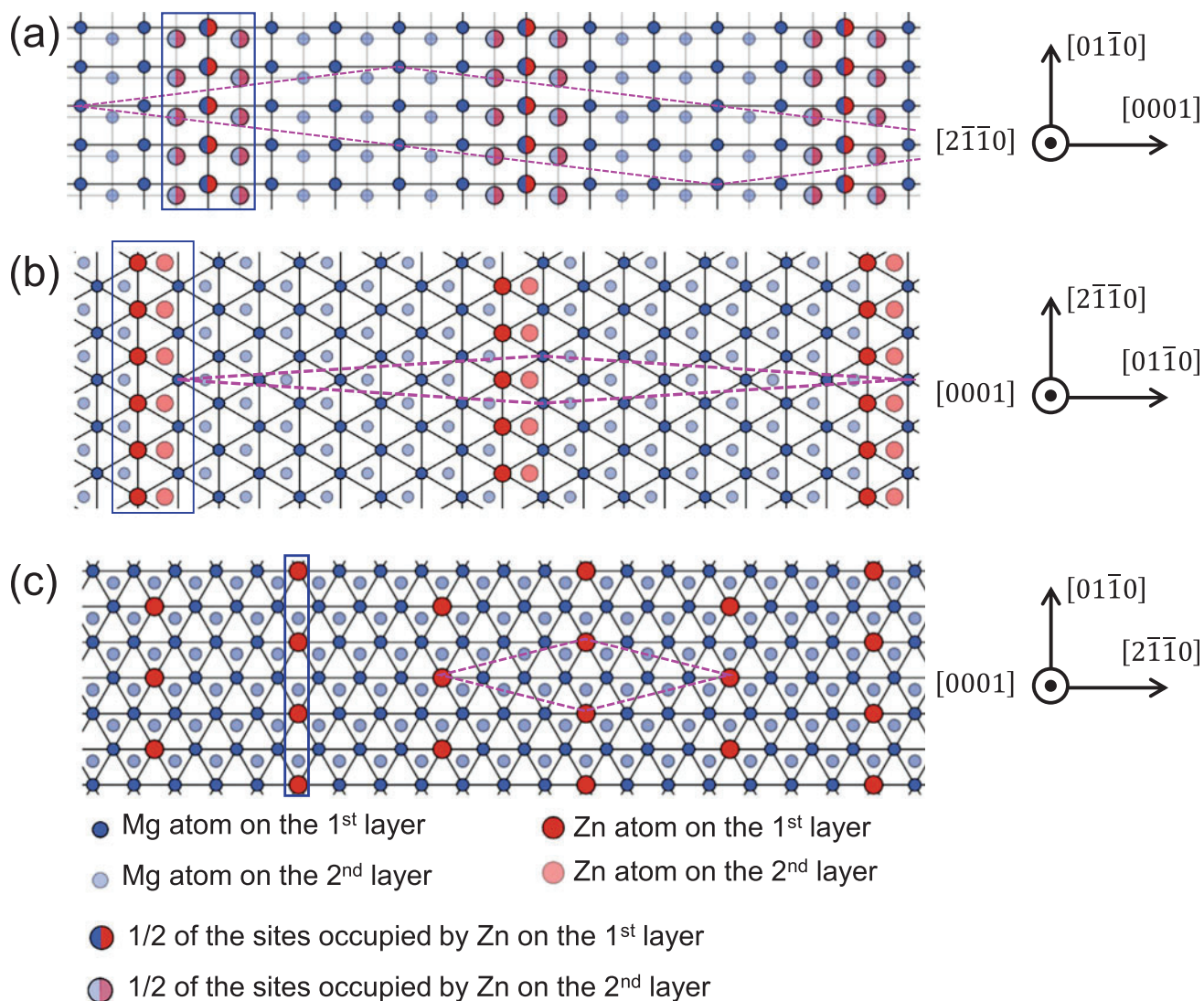


Fig. 6 Potential G.P. zones on various planes of Mg-Zn alloys: **a** $\{0001\}$ plane; **b** $\{01\bar{1}0\}$ plane; **c** $\{2\bar{1}\bar{1}0\}$ plane. The blue and red circles represent Mg and Zn atoms. The blue rectangles indicate the Zn-rich region of the G.P. zone and the pink dashed lines indicate the unit cells (Color figure online)

Discussions

A comparison of the calculations for HCP lattices of Mg-Sn and Mg-Zn alloys shows that the convergence of CE is more challenging for HCP Mg-Zn alloys. There are 228 and 385 structures included in the training of CEs for HCP Mg-Sn and Mg-Zn systems, respectively. Even with more training structures, LOOCV for CE of HCP Mg-Zn (i.e., 4.0 meV/atom) is larger than that of Mg-Sn system (i.e., 3.5 meV/atom). The corresponding cut-off distances for clusters are 7.82 and 10.09 Å for CEs of HCP Mg-Sn and Mg-Zn systems. The slow convergence of CE could be due to the long-ranged interactions, which is excluded in the CE due to the cut-off distances in cluster selections.

In alloys, a mismatch between the alloy constituents is very common and can cause long-ranged strain interactions, which is related to the long-ranged component of the force constant matrix [55]. To analyze the extent of lattice distortion required to maintain coherent configurations on HCP lattice, the epitaxial deformation energy is calculated for HCP Mg on the basal and $\{01\bar{1}0\}$ prismatic planes. For the latter, there are two independent lattice parameters on the epitaxial plane, the c/a is fixed at the equilibrium value of HCP Mg to simplify the calculations. The epitaxial deformation energy is shown in Fig. 7, where the blue dots represent DFT calculations, while the red dashed lines represent harmonic fitting to 0.95~1.05 times the equilibrium lattice parameter. The lattice parameters of Mg, Sn, and Zn are indicated by dashed vertical lines. On the basal plane, the

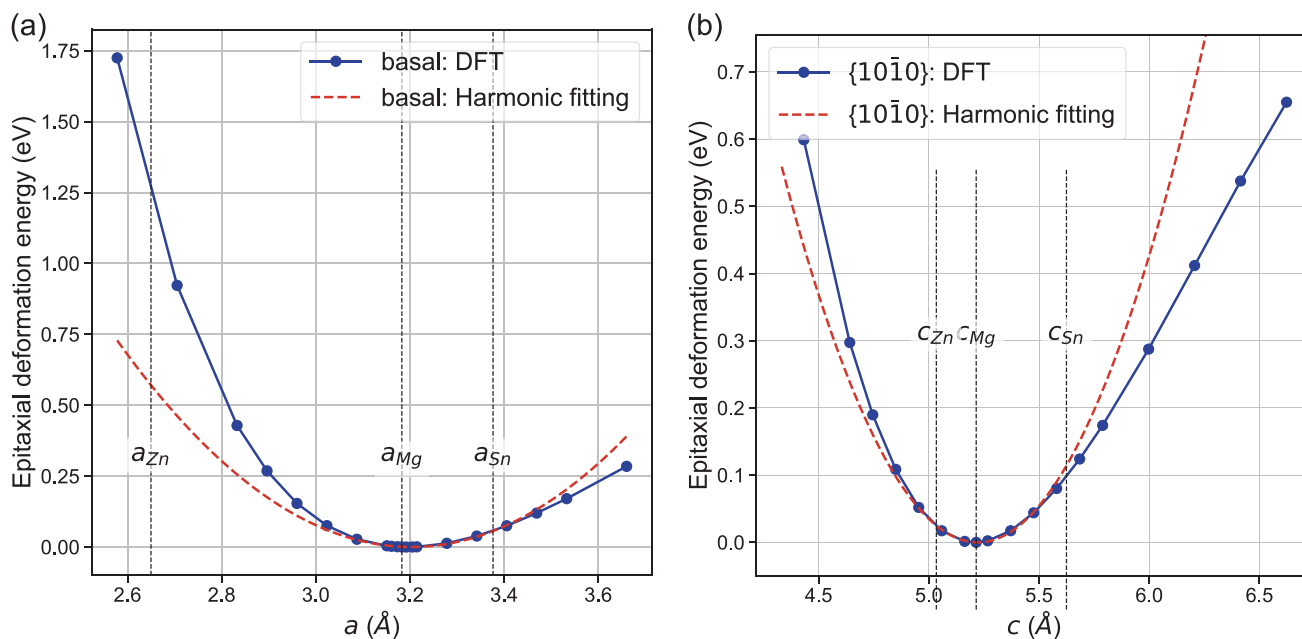


Fig. 7 Epitaxial deformation energies of the primitive cell of HCP Mg on basal (a) and $\{10\bar{1}0\}$ prismatic plane with fixed $c/a = 1.63$ (b): the deformation energies as a function of the epitaxial lattice parameters from DFT (blue line) and harmonic fitting of 0.95~1.05 times the

equilibrium lattice parameter (red dashed line) are shown. The lattice parameters of HCP Zn and Sn are also shown to indicate the amount of epitaxial deformation needed to maintain coherency (Color figure online)

lattice parameter of Sn is much closer to Mg than that of Zn. Define the lattice mismatch as $\delta = (a_X - a_{Mg})/a_{Mg}$, where X represents the solute. On basal plane, the lattice mismatch for Mg-Sn system is 6%, while that of Zn is -16.7%. Note that harmonic fitting only accounts for the harmonic response of the lattice distortion, while DFT can incorporate the non-harmonic effects. As shown for the basal plane in Fig. 7a, harmonic fitting fails to describe the deformation energy within lattice parameters of interest, and strong anharmonic distortion is needed for HCP Mg to maintain coherency with Zn, which corresponds to the case where local Zn concentration is high in Mg-Zn alloys. Meanwhile, the distortion for Mg to maintain coherency with Sn is approximately harmonic, as harmonic fitting can accurately describe the deformation energy as a function of lattice parameter. In contrast to the basal plane, the lattice mismatches along c -axis are smaller, i.e., 7.8% for Mg-Sn and -3.5% for Mg-Zn. Hence, the epitaxial deformation energy for $\{01\bar{1}0\}$ prismatic plane from DFT generally agrees with the harmonic fitting; see Fig. 7b. Therefore, it is easier for Mg to maintain coherency with Sn across all the concentration range, while strongly anharmonic distortion is needed for Mg-Zn system on the basal plane. The strain interactions resulting from the lattice mismatch can propagate to long distances and cannot be incorporated in CE, where cut-off distances are needed. Once the coherency is broken, the

local Zn-rich regions in Mg-Zn system are more likely to form incoherent precipitates, such as C14 $MgZn_2$, Mg_4Zn_7 , and $Mg_{21}Zn_{25}$.

Conclusions

In the current work, first-principles calculations based on DFT and CE are adopted to examine the structures and stabilities of precipitation phases and search for potential G.P. zones in Mg-Sn and Mg-Zn alloys. The main conclusions are as follows:

1. The potential G.P. zone on the basal plane that resembles the $D0_{19} Mg_3Sn$ phase is identified in Mg-Sn system, and the full precipitation sequence follows the supersaturated solid solution \rightarrow basal plane G.P. zones $\rightarrow D0_{19} Mg_3Sn \rightarrow L1_2 Mg_3Sn \rightarrow \beta Mg_2Sn$. The nucleation of the $L1_2$ phase in HCP matrix is likely to be facilitated by the appearance of stacking faults.
2. Current DFT calculations for Mg-Zn system agree with the experimental precipitation sequence C14 $MgZn_2 \rightarrow Mg_4Zn_7 \rightarrow Mg_{21}Zn_{25}$. Potential G.P. zones on basal, $\{10\bar{1}0\}$ and $\{2\bar{1}10\}$ planes are identified. The presence of relatively stable phases may drive the system to skip

the potential G.P. zones in aging processes, making it more challenging to observe G.P. zones experimentally.

3. Compared with Mg-Sn system, the larger lattice mismatch in Mg-Zn systems on the basal plane contributes to the long-ranged interactions, which makes it difficult for Mg lattice to maintain coherency in local regions with high Zn concentrations. And they are more likely to form incoherent precipitates in Mg-Zn alloys.

Acknowledgements This work is supported by DMREF Collaborative Research: Low cost, high strength, and ductile Mg alloys enabled by Guinier-Preston (GP) zones (No. 1921926), and the start-up funds of the University of Virginia. The authors acknowledge Advanced Research Computing Services at the University of Virginia for providing computational resources and technical support. This work also used the Extreme Science and Engineering Discovery Environment (XSEDE), which is supported by the National Science Foundation grant number ACI-1548562.

References

1. M. Esmaily, J.E. Svensson, S. Fajardo, N. Birbilis, G.S. Frankel, S. Virtanen, R. Arrabal, S. Thomas, L.G. Johansson, Fundamentals and advances in magnesium alloy corrosion, *Prog. Mater. Sci.* 89 (2017) 92–193.
2. J.F. Nie, Precipitation and hardening in magnesium alloys, *Mater. Mater. Trans. A* 43A (2012) 3891–3939.
3. N. Stanford, R. Cottam, B. Davis, J. Robson, Evaluating the effect of yttrium as a solute strengthener in magnesium using in situ neutron diffraction, *Acta Mater.* 78 (2014) 1–13.
4. Y. Chino, M. Kado, M. Mabuchi, Compressive deformation behavior at room temperature - 773 K in Mg-0.2 mass%(0.035at. %)Ce alloy, *Acta Mater.* 56 (2008) 387–394.
5. S.R. Agnew, M.H. Yoo, C.N. Tomé, Application of texture simulation to understanding mechanical behavior of Mg and solid solution alloys containing Li or Y, *Acta Mater.* 49 (2001) 4277–4289.
6. S. Sandlöbes, S. Zaeferrer, I. Schestakow, S. Yi, R. Gonzalez-Martinez, On the role of non-basal deformation mechanisms for the ductility of Mg and Mg-Y alloys, *Acta Mater.* 59 (2011) 429–439.
7. X.H. Shao, Z.Q. Yang, X.L. Ma, Strengthening and toughening mechanisms in Mg-Zn-Y alloy with a long period stacking ordered structure, *Acta Mater.* 58 (2010) 4760–4771.
8. Z. Yang, H. Ye, Dislocations in Mg alloys with rare-earth element addition, *Miner. Met. Mater. Ser. Part F7* (2018) 181–186.
9. C. Ha, S. Yi, J. Bohlen, X. Zhou, H.G. Brokmeier, N. Schell, D. Letzig, K.U. Kainer, Deformation and recrystallization mechanisms and their influence on the microstructure development of rare earth containing magnesium sheets, *Miner. Met. Mater. Ser. Part F7* (2018) 209–216.
10. K. Hantzsche, J. Bohlen, J. Wendt, K.U. Kainer, S.B. Yi, D. Letzig, Effect of rare earth additions on microstructure and texture development of magnesium alloy sheets, *Scr. Mater.* 63 (2010) 725–730.
11. J. Bohlen, M.R. Nürnberg, J.W. Senn, D. Letzig, S.R. Agnew, The texture and anisotropy of magnesium-zinc-rare earth alloy sheets, *Acta Mater.* 55 (2007) 2101–2112.
12. Y. Chino, T. Ueda, Y. Otomatsu, K. Sassa, X. Huang, K. Suzuki, M. Mabuchi, Effects of Ca on tensile properties and stretch formability at room temperature in Mg-Zn and Mg-Al alloys, *Mater. Trans.* 52 (2011) 1477–1482.
13. D.W. Kim, B.C. Suh, M.S. Shim, J.H. Bae, D.H. Kim, N.J. Kim, Texture evolution in Mg-Zn-Ca alloy sheets, *Mater. Mater. Trans. A* 44 (2013) 2950–2961.
14. S. Yi, J. Bohlen, F. Heinemann, D. Letzig, Mechanical anisotropy and deep drawing behaviour of AZ31 and ZE10 magnesium alloy sheets, *Acta Mater.* 58 (2010) 592–605.
15. H. Pan, Y. Ren, H. Fu, H. Zhao, L. Wang, X. Meng, G. Qin, Recent developments in rare-earth free wrought magnesium alloys having high strength: A review, *J. Alloys Compd.* 663 (2016) 321–331.
16. N.E.L. Saris, E. Mervaala, H. Karppanen, J.A. Khawaja, A. Lewenstam, Magnesium: An update on physiological, clinical and analytical aspects, *Clin. Chim. Acta.* 294 (2000) 1–26.
17. X. Gu, Y. Zheng, Y. Cheng, S. Zhong, T. Xi, In vitro corrosion and biocompatibility of binary magnesium alloys, *Biomaterials.* 30 (2009) 484–498.
18. A.A. Nayeb-Hashemi, J.B. Clark, The Mg-Sn (Magnesium-Tin) System Mg-Sn, *Bull. Alloy Phase Diagrams.* 5 (1984) 466–467.
19. M.A. Gibson, X. Fang, C.J. Bettles, C.R. Hutchinson, The effect of precipitate state on the creep resistance of Mg-Sn alloys, *Scr. Mater.* 63 (2010) 899–902.
20. G. Nayyeri, R. Mahmudi, Enhanced creep properties of a cast Mg–5Sn alloy subjected to aging-treatment, *Mater. Sci. Eng. A* 527 (2010) 4613–4618.
21. T.T. Sasaki, K. Oh-ishi, T. Ohkubo, K. Hono, Enhanced age hardening response by the addition of Zn in Mg–Sn alloys, *Scr. Mater.* 55 (2006) 251–254.
22. S. Harosh, L. Miller, G. Levi, M. Bamberger, Microstructure and properties of Mg-5.6%Sn-4.4%Zn-2.1%Al alloy, *J. Mater. Sci.* 42 (2007) 9983–9989.
23. C.Q. Liu, H.W. Chen, H. Liu, X.J. Zhao, J.F. Nie, Metastable precipitate phases in Mg–9.8 wt%Sn alloy, *Acta Mater.* 144 (2018) 590–600.
24. C. Liu, H. Chen, N. Wilson, J.F. Nie, Twin-like fault in Mg–9.8 wt %Sn alloy, *Scr. Mater.* 155 (2018) 89–93.
25. D.H. Kim, Y.K. Kim, D.H. Kim, W.T. Kim, Precipitation of DO19type metastable phase in Mg-Sn alloy, *Mater. Lett.* 113 (2013) 50–53.
26. L. Ye, Y. Zhuang, D. Zhao, S. Jia, J. Zhou, J. Gui, J. Wang, Transmission electron microscopy investigations of the microstructures in rapidly solidified Mg-Sn ribbons, *Micron.* 115 (2018) 1–6.
27. H. Okamoto, Supplemental literature review of binary phase diagrams: Cs-In, Cs-K, Cs-Rb, Eu-In, Ho-Mn, K-Rb, Li-Mg, Mg-Nd, Mg-Zn, Mn-Sm, O-Sb, and Si-Sr, *J. Phase Equilibria Diffus.* 34 (2013) 251–263.
28. D. Zhu, I. Cockerill, Y. Su, Z. Zhang, J. Fu, K.W. Lee, J. Ma, C. Okpokwasili, L. Tang, Y. Zheng, Y.X. Qin, Y. Wang, Mechanical strength, biodegradation, and in vitro and in vivo biocompatibility of Zn biomaterials, *ACS Appl. Mater. Interfaces.* 11 (2019) 6809–6819.
29. A. Van De Walle, Methods for first-principles alloy thermodynamics, *JOM.* 65 (2013) 1523–1532.
30. A. Van de Walle, G. Ceder, The effect of lattice vibrations on substitutional alloy thermodynamics, *Rev. Mod. Phys.* 74 (2002) 11–45.
31. A. van de Walle, M. Asta, Self-driven lattice-model Monte Carlo simulations of alloy thermodynamic properties and phase diagrams, *Model. Simul. Mater. Sci. Eng.* 10 (2002) 521–538.
32. W. Kohn, L.J. Sham, Self-Consistent Equations Including Exchange and Correlation Effects, *Phys. Rev.* 140 (1965) A1133.
33. P. Hohenberg, W. Kohn, Inhomogeneous Electron Gas, *Phys. Rev.* 136 (1964) 864.

34. Y. Mishin, M. Asta, J. Li, Atomistic modeling of interfaces and their impact on microstructure and properties, *Acta Mater.* 58 (2010) 1117–1151.
35. D. Joubert, From ultrasoft pseudopotentials to the projector augmented-wave method, *Phys. Rev. B - Condens. Matter Mater. Phys.* 59 (1999) 1758–1775.
36. J.P. Perdew, K. Burke, M. Ernzerhof, Generalized gradient approximation made simple, *Phys. Rev. Lett.* 77 (1996) 3865–3868.
37. G. Kresse, J. Furthmüller, Efficiency of ab-initio total energy calculations for metals and semiconductors using a plane-wave basis set, *Comput. Mater. Sci.* 6 (1996) 15–50.
38. G. Kresse, Efficient iterative schemes for ab initio total-energy calculations using a plane-wave basis set, *Phys. Rev. B.* 54 (1996) 11169–11186.
39. M. Methfessel, A.T. Paxton, High-precision sampling for Brillouin-zone integration in metals, *Phys. Rev. B.* 40 (1989) 3616–3621.
40. P.E. Blöchl, O. Jepsen, O.K. Andersen, Improved tetrahedron method for Brillouin-zone integrations, *Phys. Rev. B.* 49 (1994) 16223–16233.
41. D.B. Laks, L.G. Ferreira, S. Froyen, A. Zunger, Efficient cluster expansion for substitutional systems, *Phys. Rev. B.* 46 (1992) 12587–12605.
42. A. Issa, J.E. Saal, C. Wolverton, Physical factors controlling the observed high-strength precipitate morphology in Mg-rare earth alloys, *Acta Mater.* 65 (2014) 240–250.
43. V. Ozoliņš, C. Wolverton, A. Zunger, Strain-induced change in the elastically soft direction of epitaxially grown face-centered-cubic metals, *Appl. Phys. Lett.* 72 (1998) 427–429.
44. A. van de Walle, G. Ceder, Automating first-principles phase diagram calculations, *J. Phase Equilibria.* 23 (2002) 348–359.
45. A. Van de Walle, M. Asta, G. Ceder, The alloy theoretic automated toolkit: A user guide, *Calphad Comput. Coupling Phase Diagrams Thermochem.* 26 (2002) 539–553.
46. J. Buha, Reduced temperature (22–100 °C) ageing of an Mg-Zn alloy, *Mater. Sci. Eng. A.* 492 (2008) 11–19.
47. A. Bendo, T. Maeda, K. Matsuda, A. Lervik, R. Holmestad, C.D. Marioara, K. Nishimura, N. Nunomura, H. Toda, M. Yamaguchi, K. ichi Ikeda, T. Homma, Characterisation of structural similarities of precipitates in Mg-Zn and Al-Zn-Mg alloys systems, *Philos. Mag.* 99 (2019) 2619–2635.
48. A. van de Walle, Multicomponent multisublattice alloys, nonconfigurational entropy and other additions to the Alloy Theoretic Automated Toolkit, *Calphad Comput. Coupling Phase Diagrams Thermochem.* 33 (2009) 266–278.
49. K. Wang, D. Cheng, C. Fu, B. Zhou, First-principles investigation of the phase stability and early stages of precipitation in Mg-Sn alloys, *Phys. Rev. Mater.* 013606 (2020) 1–13.
50. D. Cheng, K. Wang, B.-C. Zhou, First-Principles investigations of the phase structures and stabilities in Mg-Zn alloys, to be submitted to *Acta Materialia*, 2021.
51. A.R. Natarajan, E.L.S. Solomon, B. Puchala, E.A. Marquis, A. Van Der Ven, On the early stages of precipitation in dilute Mg-Nd alloys, *Acta Mater.* 108 (2016) 367–379.
52. A.R. Natarajan, A. Van der Ven, First-principles investigation of phase stability in the Mg-Sc binary alloy, *Phys. Rev. B - Condens. Matter Mater. Phys.* 95 (2017) 214107.
53. D. Wang, M. Amsler, V.I. Hegde, J.E. Saal, A. Issa, B.C. Zhou, X. Zeng, C. Wolverton, Crystal structure, energetics, and phase stability of strengthening precipitates in Mg alloys: A first-principles study, *Acta Mater.* 158 (2018) 65–78.
54. N.C. Verissimo, C. Brito, C.R. Afonso, J.E. Spinelli, N. Cheung, A. Garcia, Microstructure characterization of a directionally solidified Mg-12wt.%Zn alloy: Equiaxed dendrites, eutectic mixture and type/ morphology of intermetallics, *Mater. Chem. Phys.* 204 (2018) 105–131.
55. D.B. Laks, L.G. Ferreira, S. Froyen, A. Zunger, Efficient cluster expansion for substitutional systems, *Phys. Rev. B - Condens. Matter Mater. Phys.* 46 (1992) 12587.